Novel method of estimation of inertial and dissipative parameters of a railway pantograph model

Andrzej Wilk, Len Gelman, Slawomir Judek, Krzysztof Karwowski, Mirosław Mizan, Tadeusz Maciołek, Miroslaw Lewandowski, Aleksander Jakubowski & Karolina Klimowska

Published online: 23 Mar 2021.

Submit your article to this journal ☐

Article views: 674

View related articles ☐

View Crossmark data ☐

IA*VSD*

Taylor & Francis
Taylor & Francis Group

Novel method of estimation of inertial and dissipative parameters of a railway pantograph model

Andrzej Wilk ⓘ[a], Len Gelman ⓘ[b], Slawomir Judek ⓘ[a], Krzysztof Karwowski ⓘ[a], Mirosław Mizan ⓘ[c], Tadeusz Maciołek ⓘ[d], Miroslaw Lewandowski ⓘ[d], Aleksander Jakubowski ⓘ[a] and Karolina Klimowska[a]

[a]Department of Electrified Transportation, Faculty of Electrical and Control Engineering, Gdańsk University of Technology, Gdańsk, Poland; [b]Department of Engineering and Technology, University of Huddersfield, School of Computing and Engineering, Queensgate, Huddersfield, UK; [c]Department of Electrical Engineering, Control Systems and Informatics, Faculty of Electrical and Control Engineering, Gdańsk University of Technology, Gdańsk, Poland; [d]Division of Electrical Traction, Electrical Power Engineering Institute, Faculty of Electrical Engineering, Warsaw University of Technology, Warsaw, Poland

ABSTRACT

An increase in electric railway vehicles service velocity requires that correct interaction between the pantograph and the catenary is ensured. This implies the need for developing mathematical models of pantographs and catenaries and determining their parameters. The article presents a method to determine parameters of mechanical joints of a railway pantograph based on analysis of pantograph subassemblies in swinging motion. The experimental tests consisted in disassembling the pantograph and creating partial subassemblies which were then analysed with respect to their damped linear or angular oscillations. The simulation analysis required developing, in CAD, 3D models of individual pantograph parts and their subassemblies. Defined were joints between particular elements, which represent of real pantograph structure. The inertia parameters of the model were determined, based on structural characteristics and physical properties of materials, used for manufacturing individual pantograph elements, and then verified experimentally. The dissipative parameters of the mechanical joints were calculated iteratively. The model of complete pantograph assembly was also subject to verification and in this case, good convergence between simulation and experiment results was achieved. The obtained parameter values can be used in simulation models of other railway pantographs having a similar structure.

1. Introduction

Models of pantographs must meet the requirements of the relevant technical standards and the Technical Specifications for Interoperability (TSI) [1–3]. A proper parametrisation of the railway pantograph model is crucial in computer simulations of dynamic interaction between the pantograph and the catenary, especially at the high speeds of an electric railway vehicle [4–6].
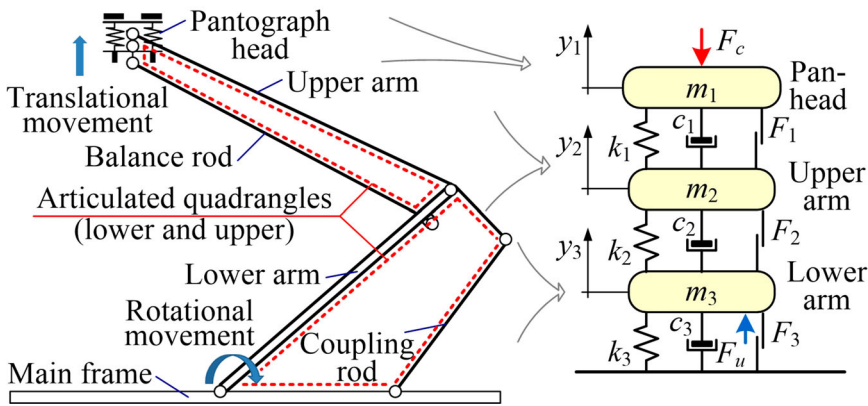
Figure 1. Railway pantograph as multibody system with two appropriate articulated quadrangles in kinematic chains and its typical equivalent model with three lumped masses.

There are two different approaches to pantograph modelling. The first consists of developing equivalent models using lumped masses, linked together by spring elements and dampers, to represent the main pantograph subassemblies which have degrees of freedom (DOF) only in translational movement. These models usually have two, three, or even four DOF [7–15]. A sample view of a pantograph and a typical scheme of its model in the mass-spring-damper arrangement are shown in Figure 1. The 2nd order differential equations with constant coefficients describe models of this type. They allow for vertical movements of pantograph elements with respect to the contact point with the catenary contact wire (see F_u, F_c in Figure 1).

These models are usually sufficient in determining the basic parameters of a pantograph–catenary interaction defined in TSI [2,3], or for instance, to define criteria for evaluating the technical condition of the pantograph for diagnostic and monitoring purposes [12,16,17]. However, for more advanced analyses, models with higher numbers of DOF are developed to take into account, for example, contact force distribution between two contact strips [8,18,19,20,21].

In some versions, a strip model is introduced in the form of a beam with a given elasticity [21–23]. Some publications suggest the use of such models for analysing the simultaneous interaction of a number of pantographs with the catenary [19,22], taking into consideration additional phenomena such as the effect of friction forces between the strips and catenary contact wires on the increase of contact force [10]. However, all these modifications reduce the main advantages of the model, which are its simplicity and easy implementation.

The basic disadvantage of the above models is that their inertia and dissipative parameters have the nature of equivalent parameters and cannot be univocally related with the inertia and dissipative parameters of real subassemblies of the pantograph. Since the structural forms of this type include DOF in both rotational and translational movements [7,24,25], the values of equivalent parameters cannot be directly measured. As a consequence, a procedure to determine the equivalent parameters for a given mathematical model should be developed. This is usually done using an iterative method until the assumed agreement is achieved between the simulation result and the experiment performed on a real pantograph [8,9,11,19,26]. As a rule, the attempt is made to reach an agreement between the spectrum characteristics of the pantograph and its model, at

appropriately selected excitations. This approach is a difficult task, and its consequence is that large differences in values of individual parameters given by different authors for the same model configuration are observed. For instance, for the three-mass model shown in Figure 1, an overview of selected publications [7,10,11,14,19,27–31] brings the following approximate ranges of parameters for masses: $m_1 = 7$–17 kg, $m_2 = 4$–18 kg, $m_3 = 5$–29 kg; for stiffness coefficients: $k_1 = 5000$–64000 N/m, $k_2 = 150$–30300 N/m, $k_3 = 1$–7250 N/m; and for damping coefficients: $c_1 = 0$–200 Ns/m, $c_2 = 0$–10 Ns/m, $c_3 = 30$–500 Ns/m. The majority of authors also neglect friction forces (F_1, F_2, F_3) which occur at particular nodes of the model shown in Figure 1. In addition, usually, aerodynamic resistance is not taken into account in the pantograph model itself, but rather is taken into consideration as an additional component of force. Considering that the above parameter values refer to different types of railway pantograph which are used for similar purposes and, therefore, have similar rated parameters, structure, and dimensions, such large differences between them suggest the possibility that similar dynamic characteristics of a given pantograph model can be obtained for various combinations of radically different values of individual parameters of this model. The lack of precise, analytical relationships between the physical parameters of the object and the particular parameters of its model makes it completely impossible to perform simulation analyses or drastically limits their accuracy in assessing the effect of possible design or operating changes introduced to a real pantograph on its interaction with the catenary [27]. As interesting examples of analyses which require more advanced models can be found in the literature, the following adjustment may be mentioned: simulation of the effect of introducing a pneumatic pantograph head suspension [32], finding the optimal location for the actuator in the automatic contact force control system (so-called active pantograph) [33] and selecting the hydraulic damper characteristic in the lower arm drive system to improve the dynamic properties of the pantograph [34].

The other approach consists of developing models with numbers of DOF corresponding to those in a real pantograph, i.e. representing the dynamics of the real system via translational and rotational movements [10,13,27,33–38]. The advantage of these models is that they take into consideration degrees of freedom taking place in a real object, along with the number and type of real mechanical joints. In many cases, they also reflect the full 3D geometry of the pantograph, which is essential when analysing proper pantograph–catenary interaction in the tension span area or places of overhead crossing [32,39].

A basic disadvantage of models which map real design and kinematic structure of a pantograph is that their mathematical formula is relatively complex and expressed by a nonlinear system of differential equations with varying parameters [34,37]. New multibody methods allow for a methodical assembly and solution of the system equations of motion, thus overcoming the difficulties in analytical approaches. These methodologies have been adopted by CAD and CAE techniques which make it possible to analyses dynamic interactions in dedicated software applications [18,21,24,27–30,38–42]. However, full modelling of the structure and characteristics of the pantograph requires determining a large number of parameters, which may amount up to several tens [34,37]. A comparison of the above presented two categories of current collector models is given in [43].

It is noteworthy that in both approaches, modelling the dynamics of a separate pantograph without its interaction with the catenary is sometimes done using popular software

such as Matlab Simulink [14,16,34,37,44,45]. On the other hand, to perform complete and reliable simulation of the pantograph(s)–catenary interaction, specialised software is developed. Concerning catenary modelling, a dominating tendency is to use the Finite Element Method (FEM) [13,18,20,21,27,29,30,35,38–40,46]. Sporadically, the Finite Difference Method (FDM) is also used [41]. With respect to pantograph modelling, it can be concluded that nearly all applications described in the literature make it possible to use a simplified type of an equivalent model consisting of a number of masses, springs, and dampers. On the other hand, more advanced applications have also implemented models that represent a real geometry and kinetics of the pantograph [30,36,39,41], and some of them take into account the elasticity of contact strips [19,21,23,36,39,41]. The majority of the software described in the literature on this subject has been collated in [28], which presents their main properties and compares results generated by them.

Also of interest, is that the pantograph–catenary interaction can be analysed using general-purpose software packages such as ANSYS [21,23] or ADAMS [47], which makes it possible to simulate the motion of complex mechanical structures. However, their use requires, as a rule, more effort to prepare the model.

When the models representing the real structure of the pantograph are used, the inertia parameters are calculated automatically in CAD and CAE software based on the structural properties of the pantograph and the physical properties of the defined materials. Nevertheless, determining dissipative parameters of joints of pantograph elements remains a problem, as these parameters depend not only on structural properties of the joint but also on viscous and elastic properties of the medium filling the space between the surfaces of the elements moving with respect to each other. In numerous analyses making use of this type of model, revolute joints are assumed as ideal, and the effect of that phenomenon on the pantograph's dynamics is neglected. Apart from the slightly decreased accuracy of the simulation analysis, in this case, the effect of change of those parameters, as a result of operating wear for instance, on the quality of pantograph–catenary interaction cannot be assessed. If the viscous and dry friction phenomena are to be taken into consideration, the usually unknown values of those parameters for individual joints should be determined by the software user using specific methods.

This article proposes a method to determine the parameters of individual joints for a typical railway pantograph. The method is based on the iterative selection of dissipative parameters of a joint and comparing the obtained simulation results with the experiment. The modelling approach based on the world-renowned CAD/CAE software was used in this work to develop a multibody model of pantograph for the purpose of determining its dissipative parameters. Following this, models of the pantograph subassemblies were developed and experimentally validated. Finally, the complete assembly of the multibody pantograph model was developed and also experimentally validated. The assumed comparison criterion was the minimisation of root mean square error (RMSE) [48].

The novel aspects of this work include:

- the method of estimation of inertial and dissipative parameters of the railway pantograph which allows for all joints in both rotational and translational motion,
- the experimental validation of the pantograph model and the estimation method of model parameters,
- an investigation of the dissipative parameters of the pantograph model.

This paper aims to achieve the following objectives:

- Developing a detailed model of the pantograph in Autodesk Inventor Software using the Dynamics Simulation Module, taking into account geometry, dimensions, mass distribution, and joints representing the real pantograph. Investigating the dissipative parameter values (dry and viscous friction) of each joint using both an experimental and analytical approach;
- Experimentally validating the pantograph model and the estimation method of model parameters.

Section 2 presents the structure of the examined pantograph, while Section 3 describes the inertia parameters of the pantograph subassemblies which affect its dynamic characteristics. Section 4 presents the issue of determining the dissipative parameters of joints of the pantograph with the use of selected CAD/CAE software, and the experimental results. The parameters of viscous and dry friction which are specific for the examined pantograph are given. The results of the simulation and experiment performed for selected pantograph subassemblies are analysed in Section 5, while Section 6 presents the summary and conclusions. The following two simplifying assumptions were taken into account in the paper:

- all revolute and cylindrical joints have no clearances;
- dry friction and viscous friction parameters are constant.

2. The pantograph and its kinematic chains

The typical single-arm pantograph which was selected for further analysis is a combination of two articulated quadrangles connected in the way shown in Figure 1 [10,24,25,27,33,34,36–38]. The two quadrangles form closed kinematic chains which represent rigid mechanical system. One element of the lower quadrangle is part of the main frame; hence the system creates a lever mechanism which makes it possible to lift the remaining pantograph elements by applying a torque to the lower arm. The action of the lower arm on the remaining components of the closed chains generates a force which presses the pantograph's contact strips against the catenary contact wire.

In railway pantographs, the pneumatic actuator [38,49] generates the force F which, transmitted via a system of cams and a flexible attachment, generates the torque T (F, α) on the lower arm (Figure 2a). Depending on the lower arm rotation angle α, the cam system introduces a different value of radius $R(\alpha)$. Figure 2a illustrates the action of force F on the lower arm. Proper selection of the cam radius values as a function of rotational angle enables achieving the required characteristic of the pantograph's static force, i.e. the dependence of the static force generated during the pantograph head's motion in an upward and downward direction on its lifting height. The force acting on the cam arm is tangential to its curvature, due to the flexible attachment applied in this pantograph drive system. The degree of freedom of the articulated quadrangles with respect to the main frame is the rotational movement. Figure 2a also shows a simple equivalent model of pneumatic actuator convolution bellows, which is the parallel system of an equivalent
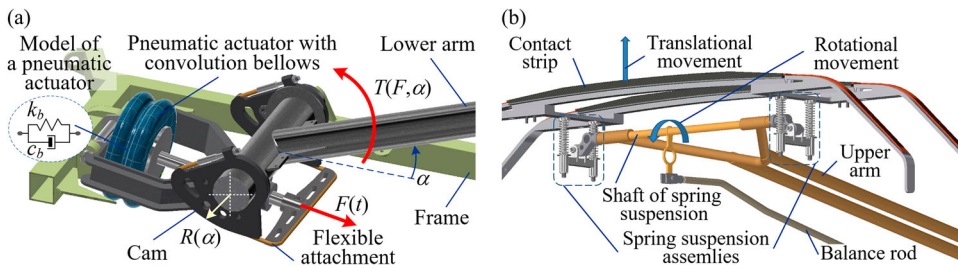
Figure 2. Pantograph subassemblies: (a) drive system, where force F generated torque $T(F, \alpha)$ acting on lower arm conducted by flexible attachment; torque T depends also on rotation angle α due to varying radius $R(\alpha)$; (b) head coupled with upper articulated quadrangle by spring suspension assemblies.

spring with elastic coefficient k_b, and an equivalent damper with viscous damping coefficient c_b.

Two spring suspension assemblies, with four springs in total, are attached to the upper quadrangle (Figure 2b). The DOF of the spring assemblies with respect to the upper arm is the rotational movement. This rotational movement is forced by the pantograph head assembly and to some small extent is free in nature, due to the clearance in the joint between the pantograph head and the spring suspension assembly shaft. The analysis of this closed chains confirms the very important role played by the pantograph head assembly. Proper positioning of this element and proper adjustment of its length ensures that the contact strips are positioned parallel to the pantograph frame, regardless of the value of the lower arm rotation angle. The pantograph head assembly is attached to the spring suspension assemblies (Figure 2b). The DOF of the pantograph head with respect to the spring suspension assembly is the translational movement.

Selected parameters of the 160EC type railway pantograph which are given by its manufacturer are shown in Table 1.

Figure 3 shows a 3D CAD model of the 160EC railway pantograph, developed in Autodesk Inventor software. In the figure, additionally marked are the closed chains components, starting from joints with the main frame, via elements $1, \ldots, 8$, with marked joints $(J_1 \div J_8)$ and with spring element (J_9), up to the pantograph head contact strips. The two articulated quadrangles are also indicated. The lower quadrangle consists of lower arm – 1, coupling rod – 2, part of upper arm – 3, and the main frame, while the upper quadrangle comprises: balance rod – 4, spring suspension shaft – 5, and parts of the lower arm – 1 and upper arm – 3. The pantograph head – 8 is attached to the suspension shaft – 5 of the upper arm – 3 in this quadrangle.

Table 1. Selected parameters of 160EC type railway pantograph [48].

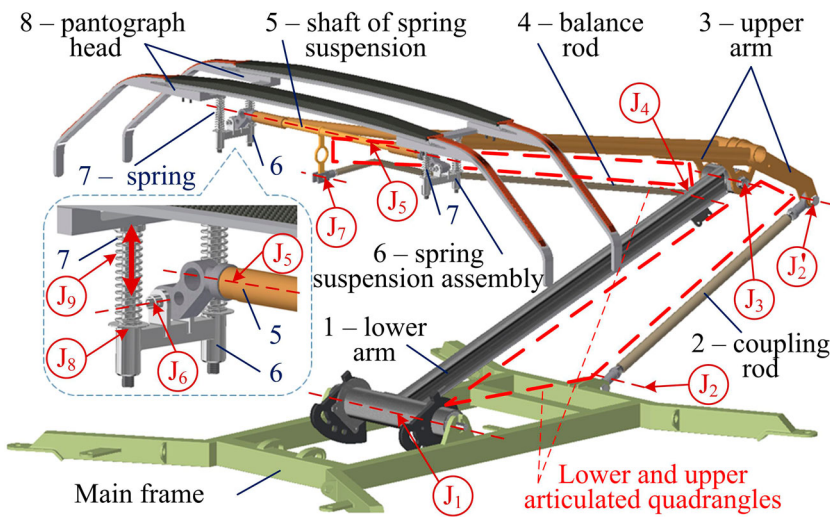| Parameters	Symbols	Data (units)
rated voltage / rated current	U_n/I_n	3 kV/1200 A
speed	v_{max}	160 km/h
static contact force	F	110 N $(-20/+10)$N
construction height min / max	h_{min} / h_{max}	300 / 2425 mm
operation height min / max	h_{min} / h_{max}	800 / 1800 mm
collector head: length x height x width	–	$1950 \times 340 \times 347$ mm
mass (without insulators)	m	125 kg
drive supply	–	pneumatic drive

Figure 3. Kinematic chains of 160EC pantograph based on two articulated quadrangles.

3. Pre-processing for pantograph modelling

3.1. Pantograph subassembly parameters

A real structure of the pantograph was expressed in the form of a 3D model in Autodesk Inventor CAD software. This made the basis for determining selected parameters for the dynamic simulation module (DSM), being part of Autodesk Inventor software, and performing validation of the pantograph motion dynamics simulation by comparing with experimental results.
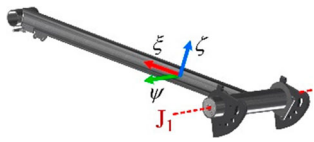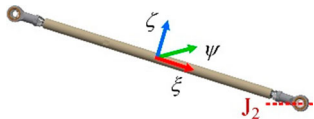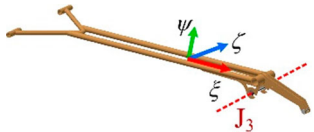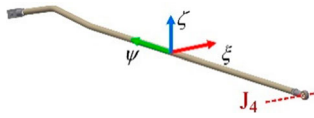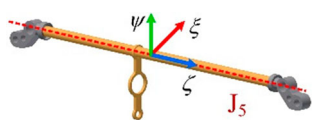
Computer models of particular pantograph parts and subassemblies and their inertia parameters, which are essential for dynamic simulations of their rotational or translational movements, are presented in Table 2. Broken lines represent axes with respect to which the moments of inertia were determined based on the 3D model. These axes correspond to those used in laboratory tests of physical pendulums. Masses, dimensions, and material properties of particular parts correspond to those of a real pantograph (Figure 3) [49].

3.2. Representation of pantograph's joints in Autodesk Inventor

Geometric constraints imposed on individual pantograph parts and their subassemblies define the mechanical properties of the pantograph, i.e. geometric relations between elements moving with respect to each other. To analyse these properties, defining individual joints and attributing values to their parameters is required. Types of joints defined in the examined 160EC pantograph are collated in Table 3, which presents the symbol of the joint, its real view, and its type defined in the Dynamic Simulation Module (DSM) of Autodesk Inventor software.

The data defined for each degree of freedom includes position- and speed-related initial conditions, elastic and damping properties, and possible position- and speed-related excitations (if they occur). The DSM module provides an opportunity to edit elastic and

Table 2. Subassemblies and parts of the pantograph and their inertial parameters.

No	Part/Subassembly		Materials of parts	Mass [kg]	Moment of inertia – J_i axis [kg·m^2]	Inertia properties [kg·m^2] $I_{\xi\xi}, I_{\psi\psi}, I_{\zeta\zeta}$	Centre of mass [m] ξ_0, y_0, z_0
1		Lower arm	Steel	18.8	5.61	0.322 4.183 4.449	0.272 0.0 −0.004
2		Coupling rod	Steel,brass	3.0	0.958	0.001 0.315 0.315	0.463 0.0 0.0
3		Upper arm	Steel	10.1	5.98	0.112 3.610 3.515	−0.542 −0.013 0.0
4		Balance rod	Steel,brass	1.85	1.64	0.417 0.0 0.417	0.0 0.802 −0.03
5		Shaft of spring suspension	Steel	1.98	$1.31 \cdot 10^{-3}$	0.159 0.158 0.001	0.0 −0.01 −0.004

(*continued*).

Table 2. Continued.
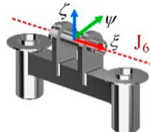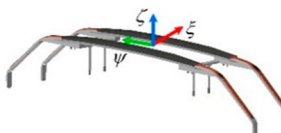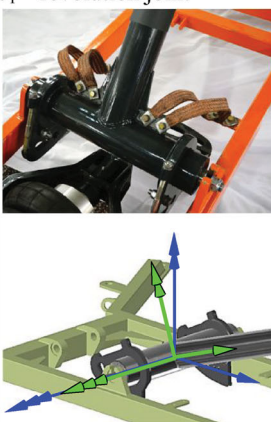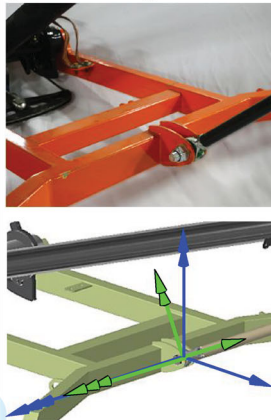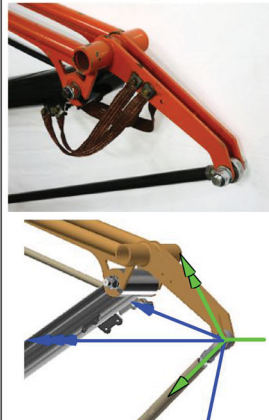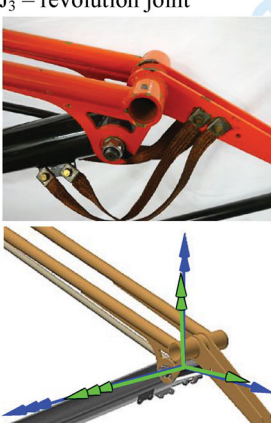
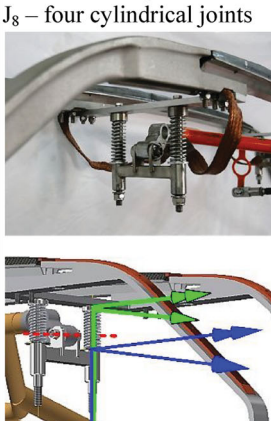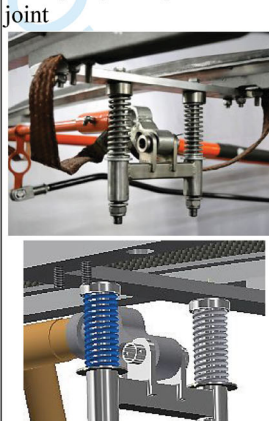| No	Part/Subassembly	Materials of parts	Mass [kg]	Moment of inertia − Ji axis [kg·m2]	Inertia properties [kg·m2] $I_{\xi\xi}, I_{\psi\psi}, I_{\zeta\zeta}$	Centre of mass [m] ξ_0, y_0, z_0
6	Spring suspension assembly	Steel	0.64	$8.27 \cdot 10^{-4}$	0.0 0.001 0.001	0.0 0.0 −0.031
7	Spring	Steel	0.063	Not applicable	–	–
8	Collector head	Steel, aluminium, copper, electrographite	16.5	Not applicable	4.360 0.463 4.495	0.0 0.0 −0.014

Table 3. Views of particular joints of 160EC pantograph and their representations in Dynamic Simulation Module of Autodesk Inventor.

J_1 – revolution joint	J_2 – revolution joint	J_2' – revolution joint

J_3 – revolution joint	J_4 – revolution joint	J_5 – revolution joint

J_7 – point–line joint	J_6 – revolution joint, J_8 – four cylindrical joints	J_9 – Spring/Damper/Jack joint

damping properties using a dialogue box. The dissipative properties of a joint include viscous and dry friction. These two phenomena can be defined as linear or nonlinear in nature. In the nonlinear case, there is a possibility to make the friction parameters dependent on the state variables of the dynamic system. These parameters can also be functions of active external forces and torques, passive reaction forces, and time. The methods to determine dissipative parameters of joints of the 160EC pantograph and the obtained laboratory results are discussed in the next section.

4. Determining dissipative parameters of joints

4.1. Experimental test stand

The block diagram of the procedure applied to determine the dissipative parameters of the pantograph subassemblies is shown in Figure 4. The diagram includes both a simulation and an experimental approach. In the experimental approach, partial connections of selected subassemblies or parts were created to enable experimental examination of an individual mechanical joint, while the simulation consisted of creating the 3D model of a selected joint and performing its simulations in conditions corresponding to those in which the object was examined experimentally (axis of revolution, initial conditions, applied excitations, etc.). Then, the results of the simulations were compared with the experiment in an iterative loop. The iteration process was terminated when the assumed RMSE value was obtained. The initial parameters introduced to the iterative loop were estimated by matching the results of measurements with the analytical solution of a differential equation describing the physical pendulum corresponding to the selected subassembly. The analysis was based on the assumption that the model includes dry and viscous friction with constant parameters. The Levenberg Marquardt algorithm was used for the calculations in Matlab [14,48].

On the test stand, basic pantograph elements were disassembled, and then their damped motion was measured in a simple physical pendulum system. For the pantograph head suspension assembly, the tests was performed for translational motion. The adopted methodology resulted from a relative simplicity of description of phenomena taking place in the pendulum system. The angular motion was recorded indirectly, using a laser distance metre to measure linear displacements against a fixed reference point. Scaling the test rig was done using an inclinometer. When necessary, an element was additionally loaded with standard weights of known dimensions and mass. The view of the measuring system
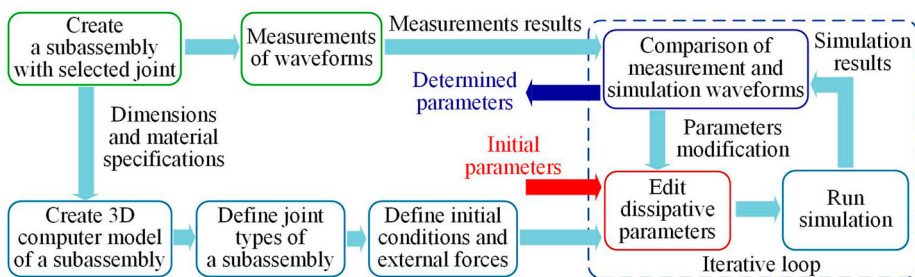

Figure 4. Task workflows for determining dissipative parameter values of the tested joint.
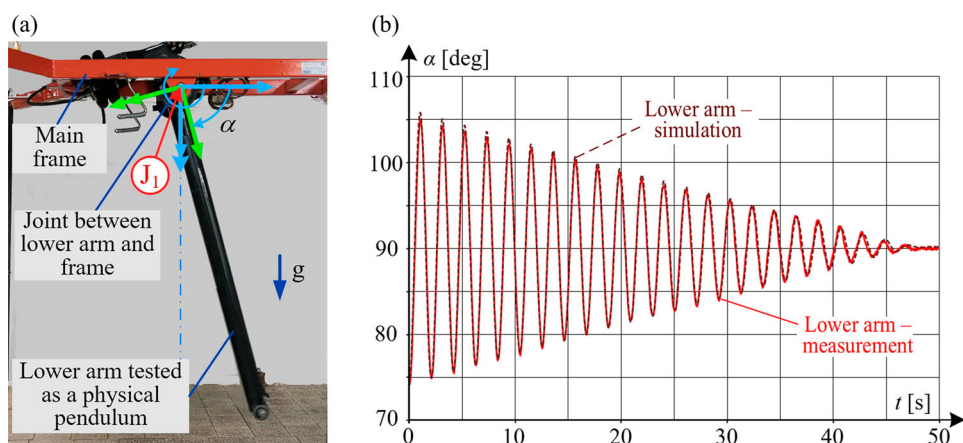
(a) (b)

Figure 5. Test of joint between lower arm and frame: (a) view of lower arm tested in the laboratory as a physical pendulum in gravitational field; (b) comparison of measurement and simulation results as revolution angles $\alpha(t)$ waveform. Initial conditions: $\alpha_0 = 74.2°$, $\omega_0 = 0$.

for testing properties of the lower arm and a subassembly of lower and upper arms and a coupling rod are shown in Figure 5a and Figure 13a, respectively.

4.2. Dissipative parameters of joints

This section presents the results of laboratory tests and simulations recorded for each individual pantograph joint, from J_1 to J_9. Friction parameters for these joints are collated in Table 4.

The friction model used in simulation in translational movement is given by

$$F(\dot{x}) = D_{vis}\dot{x} + N\mu sign(\dot{x})$$

Table 4. Characteristic features of 160EC pantograph joints and their dissipative parameters.

No. of joint	Short description of real construction features of the joint	Viscous damping coefficient	Dry friction coefficient [–]
J_1	Revolution joint of lower arm with main frame mounted on two ball bearings.	0.034 N·m·s/rad	0.023 ($R = 0.05$ m)
$J_2 J_2'$	Revolution joint J_2 of coupling rod with main frame. Revolution joint J_2' of coupling rod with upper arm. Joints J_2 and J_2' have the same ball joints with slide bearings.	0.115 N·m·s/rad	0.027 ($R = 0.01$ m)
J_3	Revolution joint of lower arm with upper arm mounted on two ball bearings.	0.017 N·m·s/rad	0.20 ($R = 0.022$ m)
J_4	Revolution joint of lower arm with balance rod. Single ball joint and slide bearing.	0.011 N·m·s/rad	0.34 ($R = 0.006$ m)
J_5	Revolution joint having two slide bearings.	0.401 N·m·s/rad	0.88 ($R = 0.01$ m)
J_6	Revolution joint of spring suspension shaft to spring suspension assembly. Slide bearings with significant clearance.	0.001 N·m·s/rad	0.14 ($R = 0.008$ m)
J_7	Revolution joint with significant clearance. Damping parameters at rotational movement are given.	0.013 N·m·s/rad	0.16 ($R = 0.007$ m)
J_8	Cylindrical joint J_8 with significant clearance. There are four such joints.	0.99 N·s/m	0.5
J_9	Spring/Damper/Jack joint J_9. Stiffness $k = 4.0$ N/mm. There are four such joints	3.0 N·s/m	–

where F is friction force, N is pressure force, $\dot{x}$ is velocity, and D_{vis} is the damping coefficient.

The friction model used in simulation in rotational movement is given by

$$T(\dot{\omega}) = D_\omega\dot{\omega} + NR\mu\ sign(\dot{\omega})$$

where T is friction torque, N is pressure force, $\dot{\omega}$ is velocity, D_ω is damping coefficient and R is radius.

The revolute joint J_1 (lower arm – main frame) and the assembly of elements for its experimental examination are shown in Figure 5a. The assembly was tested using a physical pendulum swinging in the gravitational field, at initial deflection α_0 and initial angular speed ω_0. The waveform of pantograph arm revolution angle, $\alpha(t)$ was recorded during this experiment. The comparison between the obtained simulation and the measurement results is given in Figure 5b.

The revolute joint J_2 (upper arm coupling rod – main frame) and the conditions of the laboratory test performed in the physical pendulum system for this case are shown in Figure 6a. The waveform of the coupling rod revolution angle $\alpha(t)$ was recorded in this test. Good matching was obtained with respect to the frequency of oscillations as well as satisfactory accordance with respect to the amplitude values (Figure 6b). Larger differences, observed for small-amplitude oscillations, were most likely caused by complex twisting movements in the ball joint and their effect on the measured result.

For the revolute joint J_2' (upper arm coupling rod – upper arm), the same viscous and dry friction parameters were assumed as for joint J_2 (upper arm coupling rod – main frame), as the diameters and materials of the elements as well as other properties were the same in both joints.

The revolute joint J_3 (lower arm – upper arm) and the assembly of elements for its laboratory test performed in the physical pendulum system are shown in Figure 7a. The waveform of the upper arm revolution angle $\alpha(t)$ was observed during this test. The results of both the simulation and experiment are shown in Figure 7b.
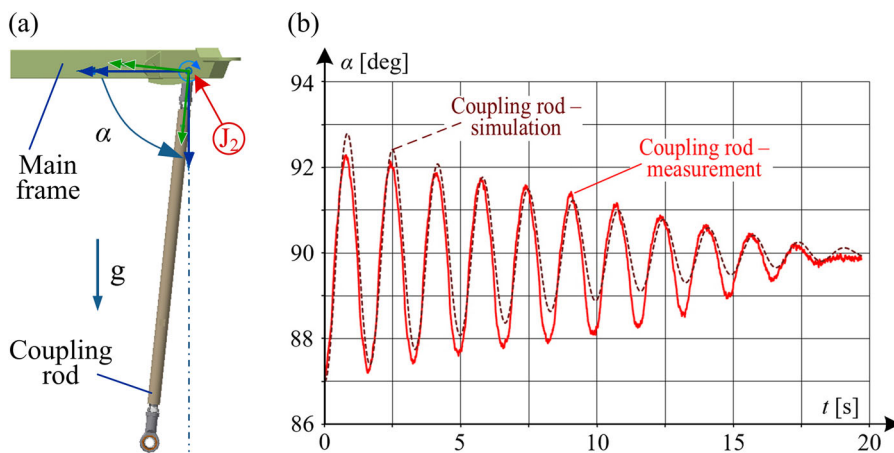

Figure 6. Test of joint between coupling rod and frame: (a) view of joint revolution in gravitational field; (b) comparison of measurement and simulation results as revolution angles $\alpha(t)$ waveform. Initial conditions: $\alpha_0 = 87.0°$, $\omega_0 = 0$.
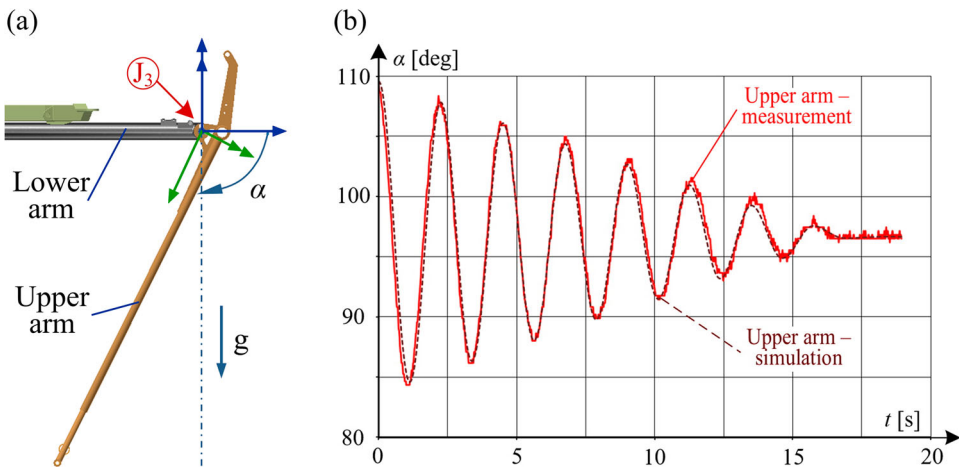
(a) (b)

Figure 7. Test of joint between lower arm and balance rod: (a) view of joint revolution in gravitational field; (b) comparison of measurement and simulation results as revolution angles $\alpha(t)$ waveform. Initial conditions: $\alpha_0 = 70.2°$, $\omega_0 = 0$.
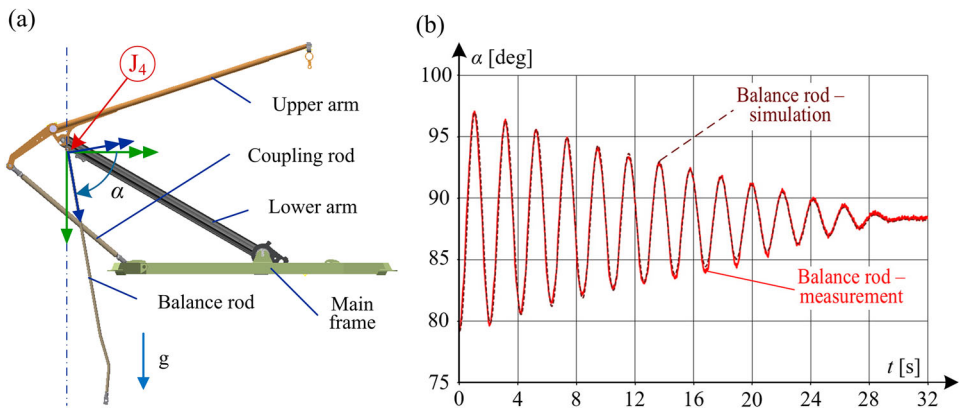
(a) (b)

Figure 8. Test of joint between spring suspension shaft and upper arm (a) view of joint revolution in gravitational field; (b) comparison of measurement and simulation results as revolution angles $\alpha(t)$ waveform. Initial conditions: $\alpha_0 = 73.3°$, with respect to horizontal reference line on horizontal plane, $\omega_0 = 0$.

The revolute joint J_4 (lower arm – balance rod) and conditions of its laboratory test are shown in Figure 8a. The waveform of the balance rod revolution angle $\alpha(t)$ was analysed in this test. The results of both the simulation and experiment are shown in Figure 8b.

The revolute joint J_5 (upper arm – spring suspension shaft) and the assembly scheme of pantograph elements for this test are shown in Figure 9a. The waveform of the spring suspension shaft revolution angle $\alpha(t)$ was measured during this experiment. To obtain a larger number of oscillations, an aluminium rod of mass 0.435 kg and length 0.95 m was attached to the shaft. Moreover, an additional weight of mass 5 kg was attached to the end of the rod. The results of both the simulation and measurements are shown in Figure 9b.
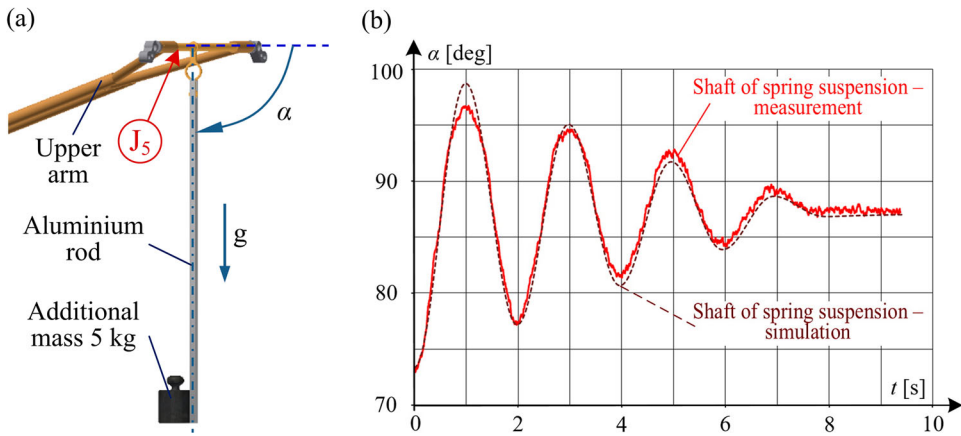
Figure 9. Test of joint between spring suspension shaft and spring suspension assembly: (a) view of joint revolution in gravitational field; (b) comparison of measurement and simulation results as revolution angles $\alpha(t)$ waveform. Initial conditions: $\alpha_0 = 103.0°$, $\omega_0 = 0$.
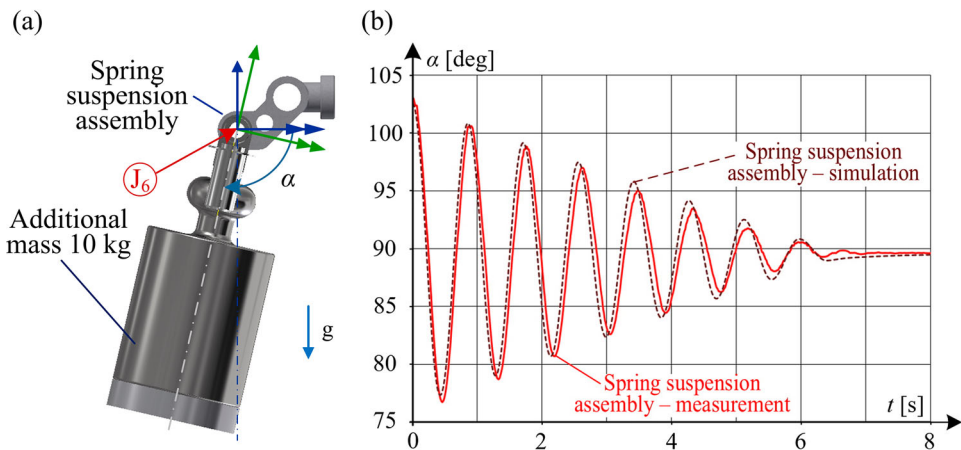

Figure 10. Test of joint between spring suspension shaft and balance rod: (a) view of joint revolution in gravitational field; (b) comparison of measurement and simulation results as revolution angles $\alpha(t)$ waveform. Initial conditions: $\alpha_0 = 79.0°$, $\omega_0 = 0$.

The joint J_6 (spring suspension shaft – spring suspension assembly) and conditions of its laboratory test are shown in Figure 10a. The waveform of the spring suspension assembly revolution angle $\alpha(t)$ was recorded in this test. To obtain a larger number of oscillations, a weight of mass 10 kg was attached to the subassembly. The results of the test are shown in Figure 10b.

The joint J_7 (spring suspension shaft–balance rod) and conditions of the laboratory test are shown in Figure 11a. The waveform of the balance rod revolution angle $\alpha(t)$ was observed during this experiment. The results of the test are shown in Figure 11b.

The joints J_8 (spring suspension unit – slider assembly pivot) and J_9 (spring) as well as the assemblies of elements for this test are shown in Figure 12a. The waveform of the pivot displacement $h(t)$ was measured in this test. Figure 12b shows the comparison of both the
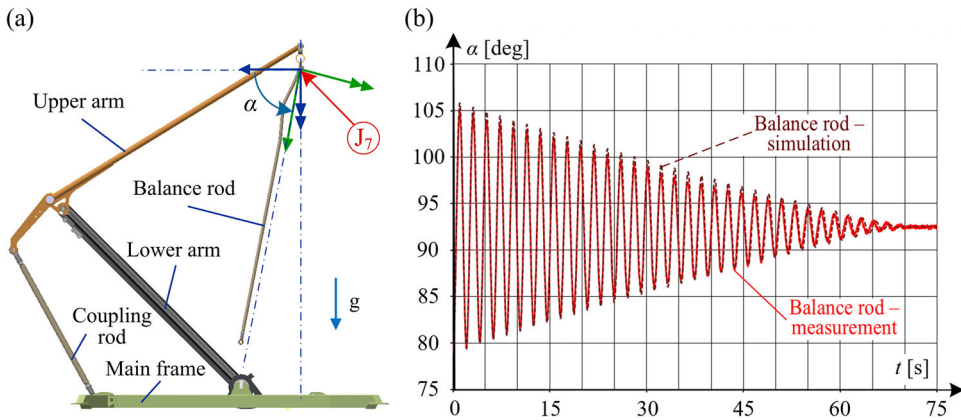
(a)

(b)

Figure 11. Test of joint between spring suspension unit and slider assembly pivot: (a) view of cylindrical joint in gravitational field; (b) comparison of measurement and simulation results as pivot displacements $h(t)$ waveform. Initial conditions: $h_0 = 73.3$ mm, $v_0 = 0$.
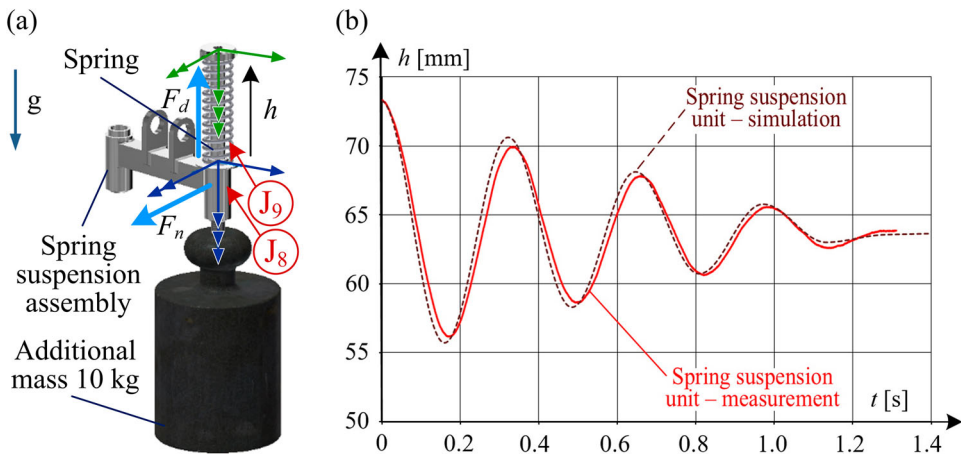
(a)

(b)

Figure 12. Test of lower articulate quadrangle: (a) view of subassembly of four joints in laboratory test stand; (b) simulation and experimental results of the subassembly oscillations. Initial conditions: $\alpha_0 = -10.1°$, $\beta_0 = -3.6°$ with respect to the pantograph frame plane inclined to horizontal plane at $\gamma = 70.0°$, $\omega_0 = 0$.

simulation and measurement results. To obtain a larger number of oscillations, the pivot was additionally weighted with a mass of 10 kg.

Despite the presence of a relatively large design clearance between the pivot and the sleeve, some effects of dry friction in joint J_8 were observed in the measurements. To consider this effect, a simplifying assumption was adopted that the dry friction force F_d is constant in magnitude but differs in a direction depending on the speed sign. Introducing into the simulation model the new force F_n directed normally to the friction surfaces and defined by the relationship $F_d = \mu \cdot F_n$, where μ is the dry friction coefficient, made it possible to take into account the friction coefficient in the oscillation damping process. The results of the simulation are shown in Figure 12b for $F_n = 4.05$ N and $\mu = 0.5$ (typical values for dry steel surfaces).

Table 4 presents characteristic features of particular joints of the 160EC pantograph and the dissipative parameters attributed to them. The two last columns show the experimentally obtained values of viscous damping coefficient and dry friction coefficient for joints marked in accordance with Figure 3. For revolute joints, the value of radius R defining the contact surface position of the cooperating elements is also given.

5. Simulation of selected dynamic states of the pantograph and experimental verification

The results of simulations shown in Sections 3 and 4 for individual joints revealed good agreement with the experiment for both the dissipative and inertia parameters of the analysed pantograph. However, the dynamic parameters of the pantograph depend, generally, on the interaction of all joints, therefore, experimental verification was performed to assess the quality of interaction of selected partial subassemblies and the operation of the complete pantograph assembly. The assemblies being the object of experimental verification were as follows:

- subassembly comprising the lower articulated quadrangle – cooperation of joints J_1, J_2, J_3, and J_4.
- subassembly comprising the pantograph head unit – cooperation of joints J_6, J_8, and J_9.
- complete assembly – pantograph together with pneumatic drive.

5.1. Subassembly comprising lower articulated quadrangle

The tested subassembly, comprising articulated joints of frame, lower arm, upper arm coupling rod, and upper arm, is shown in Figure 13a. Starting from initial deflection, the subsystem was swinging without additional external excitations. Figure 13b presents the comparison between the simulated and experimentally recorded results.
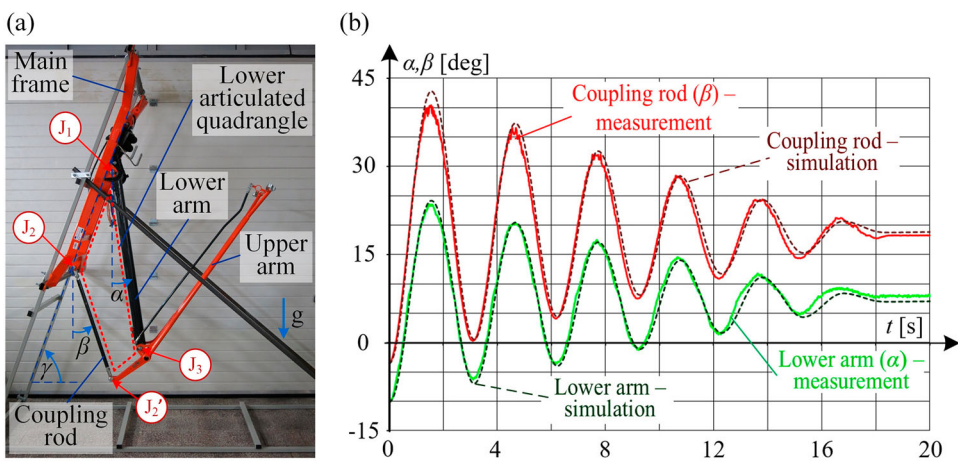

Figure 13. Test of pantograph head: (a) pantograph head with rapidly reduced vertical force F_z acting on contact strips; (b) simulation and experimental results of pantograph head displacement in the subassembly. Initial conditions: $F_z = 98.1$ N, $h_0 = 74$ mm, $\omega_0 = 0$.

5.2. Subassembly comprising pantograph head unit

This test concerned oscillations of the pantograph head unit with respect to the fixed upper and lower arm (Figure 14a). The value of the stationary initial position resulted from the action of the force of gravity and the additional external force F_z coming from the weight of mass 10 kg suspended on a flexible connecting cord from the pantograph unit. This connecting cord was then rapidly cut across to excite the almost stepwise reduction of force F_z to zero, with subsequent pantograph head oscillations. The results of the measurements and simulations are shown in Figure 14b. A good agreement was obtained with respect to vertical pantograph head displacements in the large-amplitude range. More significant differences, observed only for relatively small displacements, most likely result from the simplifying assumption adopted in the pantograph model, which says that all four joints J_8 have the same DOF. In a real pantograph, relatively large clearances occur in each J_8 joint which causes that their dynamics is more complex. The effect of clearances in these joints was not analysed in this work.

5.3. Complete pantograph assembly

Tests of the complete pantograph assembly took into consideration the joints which have their place in the real object, together with the pneumatic drive. The pantograph model includes all joints shown in Figure 3 and the model of pneumatic drive (Figure 2a), represented by a parallel connection of an equivalent spring and an equivalent damper.

At a given initial time $t = 0$, the pantograph head position height was $H_0 = 1.04$ m. Along with the force of gravity, the following forces and torques acted on its arms (Figure 15a): torque $T_0 = 1110$ Nm generated by the pneumatic drive to lift the pantograph arms, force $F_s = 18$ N coming from the external spring and used for lowering the pantograph arms, and force $F_m = 78.5$ N coming from an additional mass suspended from the pantograph head unit and used to lower its arms.

After sudden removal of force F_m (cutting off the weight of mass $m = 8$ kg), the transient stage began, which lasted less than 5 s. The steady-state parameter values were
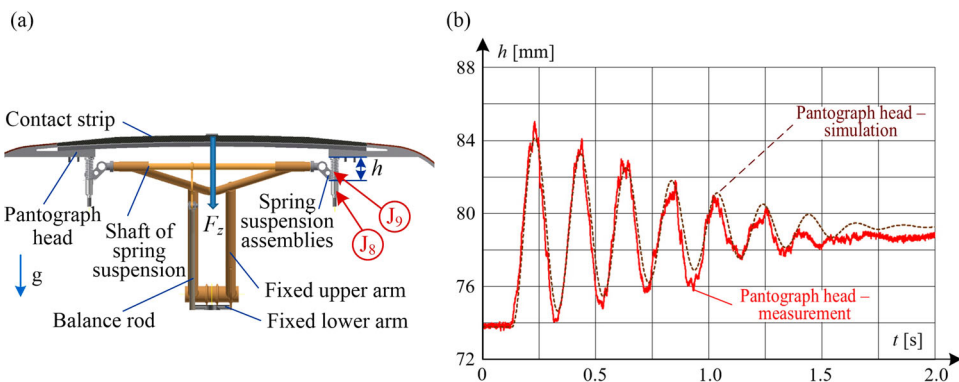

Figure 14. Test of pantograph head: (a) pantograph head with rapidly reduced vertical force F_z acting on contact strips; (b) simulation and experimental results of pantograph head displacement in the subassembly. Initial conditions: $F_z = 98.1$ N, $h_0 = 74$ mm, $\omega_0 = 0$.
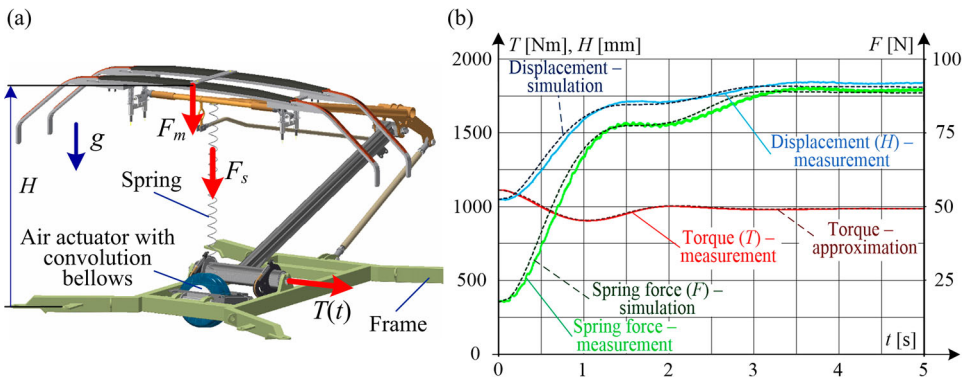
Figure 15. Test of the complete pantograph: (a) forces and torque acting on pantograph; (b) simulation and experimental results.

as follows: $H = 1.84\,\text{m}$, $T = 986\,\text{Nm}$, $F_s = 89.5\,\text{N}$, $F_m = 0$. The quantities measured during the laboratory test were H, T, and F_s. The waveforms of these parameters from measurement and simulation are shown in Figure 15b.

For simulation purposes, the measured torque $T(t)$ was approximated using an analytical function. As can be seen in Figure 15b, this approximation correctly projects the measured torque waveform.

The structure of the pneumatic drive unit is complex. Along with the pneumatic drive, it includes the pressure and airflow control systems. This unit was modelled using a simple model consisting of an equivalent spring and an equivalent damper (Figure 2a). In the simulation process, the spring and damper parameters are additional unknown parameters, therefore, their values were determined iteratively. The value of the elasticity coefficient k_b was assumed as constant, while the damping coefficient c_b was expressed by a nonlinear function dependent on the speed of the pneumatic drive piston rod. This model ensured good matching of the simulation results to the measurements. A more accurate assessment of detailed parameters of individual components of the pneumatic drive model would require taking into consideration the model of its control system. This problem requires further, more advanced research.

6. Conclusions

This work proposes and investigates the novel method of estimation of inertia and dissipative parameters, determined for a standard single–arm railway pantograph that allows for all mechanical joints in both rotational and translational motion. The inertia parameters, relative to a specific axis of rotation, were determined with the support of CAD programme. The proposed method for identifying dissipative parameters consists of disassembling the pantograph to a status for which examining individual joints is possible and then determining the dissipative parameters experimentally for individual joints on a simple test stand. In addition to the experimental tests, an estimation of the dissipative parameters was performed using a Dynamic Simulation Module (DSM), implemented in CAD software. These experimental tests and analysis have revealed that the dissipative parameter values, experimentally determined individually for a single joint, are well matched with the

References

[1] European Committee for Electrotechnical Standardization (CENELEC). Railway applications. current collection systems. validation of simulation of the dynamic interaction between pantograph and overhead contact line. Brussels: CENELEC; 2018; Standard No. EN 50318.

[2] European Committee for Electrotechnical Standardization (CENELEC). Railway applications. current collection systems. technical criteria for the interaction between pantograph and overhead line. Brussels: CENELEC; 2012; Standard No. EN 50367.

[3] Commission Implementing Regulation (EU) 2019/776 of 16 May 2019 amending Commission Regulations (EU) No. 321/2013, (EU) No. 1299/2014, (EU) No. 1301/2014, (EU) No. 1302/2014, (EU) No. 1303/2014 and (EU) 2016/919 and Commission Implementing Decision 2011/665/EU as regards the alignment with Directive (EU) 2016/797 of the European Parliament and of the Council and the implementation of specific objectives set out in Commission Delegated Decision (EU) 2017/1474 OJ L 139I, 27.5.2019, p. 108–311.

[4] Bruni S, Bucca G, Carnevale M, et al. Pantograph–catenary interaction: recent achievements and future research challenges. Int J Rail Transp. 2018;6(2):57–82.

[5] Kießling F, Puschmann R, Schmieder A, et al. Contact lines for Electric railways: planning, design, implementation, maintenance. Third, completely revised and enlarged edition. Erlangen: Wiley VCH; 2018.

[6] Zhang W, Zou D, Tan M, et al. Review of pantograph and catenary interaction. Front Mech Eng. 2018;13(2):311–322.

[7] Zhou N, Zhang W. Investigation on dynamic performance and parameter optimization design of pantograph and catenary system. Finite Elem Anal Des. 2011;47(3):288–295.

[8] Abdullah MA, Michitsuji Y, Nagai M, et al. System identification of railway trains pantograph for active pantograph simulation. J Syst Des Dyn. 2011;5(5):1141–1154.

[9] Lee JH, Park TW, Oh HK, et al. Analysis of dynamic interaction between catenary and pantograph with experimental verification and performance evaluation in new high-speed line. Veh Syst Dyn. 2015;53(8):1117–1134.

[10] Chen G, Yang Y, Yang Y. Prediction of dynamic characteristics of a pantograph-catenary system using the displacement compatibility. J Vibroengineering. 2017;19(7):5405–5420.

[11] Ambrósio J, Pombo J, Pereira M. Optimization of high-speed railway pantographs for improving pantograph-catenary contact. Theor Appl Mech Lett. 2013;3(1):013006.

[12] Xin T, Roberts C, Weston P, et al. Condition monitoring of railway pantographs to achieve fault detection and fault diagnosis. Proc Inst Mech Eng Part F J Rail Rapid Transit. 2020;234(3):289–300.

[13] Zhao C, Zhou N, Zou H, et al. Comparison of dynamic characteristics of different pantograph models. 2016 35th Chinese Control Conference (CCC); IEEE; 2016, p. 10216–10221.

[14] Judek S. Modelowanie współpracy odbieraka prądu z siecią trakcyjną. [Modelling of the pantograph–catenary interaction]. Przegląd Elektrotechniczny. 2015;1(11):251–255. Polish.

[15] Nåvik P, Rønnquist A, Stichel S. Variation in predicting pantograph–catenary interaction contact forces, numerical simulations and field measurements. Veh Syst Dyn. 2017;55(9):1265–1282.

[16] Karwowski K, Mizan M, Karkosiński D. Monitoring of current collectors on the railway line. Transport. 2016;33(1):177–185.

[17] Jarzebowicz L, Judek S. 3D machine vision system for inspection of contact strips in railway vehicle current collectors). 2014 International Conference on Applied Electronics; IEEE; 2014, p. 139–144.

[18] Cho YH. SPOPS statement of methods. Veh Syst Dyn. 2015;53(3):329–340.

[19] Bucca G, Carnevale M, Collina A, et al. Adoption of different pantographs' preloads to improve multiple collection and speed up existing lines. Veh Syst Dyn. 2012;50(sup1):403–418.

[20] Benet J, Cuartero N, Cuartero F, et al. An advanced 3D-model for the study and simulation of the pantograph catenary system. Transp Res Part C Emerg Technol. 2013;36:138–156.

[21] Jönsson P-A, Stichel S, Nilsson C. CaPaSIM statement of methods. Veh Syst Dyn. 2015;53(3):341–346.

[22] Liu Z, Jönsson P-A, Stichel S, et al. On the implementation of an auxiliary pantograph for speed increase on existing lines. Veh Syst Dyn. 2016;54(8):1077–1097.

[23] Song D, Jiang Y, Zhang W. Dynamic performance of a pantograph–catenary system with consideration of the contact surface. Proc Inst Mech Eng Part F J Rail Rapid Transit. 2018;232(1):262–274.

[24] Wilk A. Novel analysis methods of dynamic properties for vehicle pantographs. szeląg A, Karwowski K, Gold H, Żurkowski A, eds. MATEC Web Conf. 2018;180:01005.

[25] Wilk A, Judek S, Karwowski K, et al. Modal analysis of railway current collectors using Autodesk Inventor. Szeląg A, Karwowski K, Gold H, Żurkowski A, eds. MATEC Web Conf. 2018;180:04004.

[26] Wilk A, Karwowski K, Judek S, et al. A new approach to determination of the two-mass model parameters of railway current collector. 12th International Conference Modern Electrified Transport; MET'2015; Croatia, Trogir, 2015; October 4–7, p. 164–170.

[27] Antunes P, Ambrósio J, Pombo J, et al. A new methodology to study the pantograph–catenary dynamics in curved railway tracks. Veh Syst Dyn. 2020;58(3):425–452.

[28] Bruni S, Ambrosio J, Carnicero A, et al. The results of the pantograph–catenary interaction benchmark. Veh Syst Dyn. 2015;53(3):412–435.

[29] Ikeda M. 'Gasen-do FE' statement of methods. Veh Syst Dyn. 2015;53(3):357–369.

[30] Zhou N, Lv Q, Yang Y, et al. 'Gasen-do FE' statement of methods. Veh Syst Dyn. 2015;53(3):380–391.

[31] Smerdin A, Demin Y, Ryzhkov A. Improvement of the method of calculation of the parameters of the universal current collector with the increased motion speeds. Abramov AD, murgul V, eds. MATEC Web Conf. 2018;239:01040.

[32] Massat J-P, Laurent C, Bianchi J-P, et al. Pantograph catenary dynamic optimisation based on advanced multibody and finite element co-simulation tools. Veh Syst Dyn. 2014;52(sup1):338–354.

[33] Song Y, Ouyang H, Liu Z, et al. Active control of contact force for high-speed railway pantograph-catenary based on multi-body pantograph model. Mech Mach Theory. 2017;115:35–59.

[34] Wang W, Liang Y, Zhang W, et al. Effect of the nonlinear displacement-dependent characteristics of a hydraulic damper on high-speed rail pantograph dynamics. Nonlinear Dyn. 2019;95(4):3439–3464.

[35] Pombo J, Ambrósio J. Influence of pantograph suspension characteristics on the contact quality with the catenary for high speed trains. Comput Struct. 2012;110-111:32–42.

[36] Ambrósio J, Rauter F, Pombo J, et al. A flexible multibody pantograph model for the analysis of the catenary–pantograph contact. In: Arczewski K, Blajer W, Fraczek J, et al., editors. Multibody dynamics. Vol 23. Computational methods in applied sciences. Barcelona: Springer; 2011. p. 1–27.

[37] Pappalardo CM, De Simone MC, Guida D. Multibody modeling and nonlinear control of the pantograph/catenary system. Arch Appl Mech. 2019;89(8):1589–1626.

[38] Ambrósio J, Pombo J, Pereira M, et al. Recent developments in pantograph-catenary interaction modelling and analysis. Int J Railw Technol. 2012;1(1):249–278.

[39] Massat J-P, Balmes E, Bianchi J-P, et al. OSCAR statement of methods. Veh Syst Dyn. 2015;53(3):370–379.

[40] Sánchez-Rebollo C, Carnicero A, Jiménez-Octavio JR. CANDY statement of methods. Veh Syst Dyn. 2015;53(3):392–401.

[41] Finner L, Poetsch G, Sarnes B, et al. Program for catenary–pantograph analysis, PrOSA statement of methods and validation according EN 50318. Veh Syst Dyn. 2015;53(3):305–313.

[42] Pombo J, Ambrósio J, Antunes P, et al. Pantocat statement of method. Veh Sys Dyn. 2015;53(3):314–328.

[43] Kia SH, Bartolini F, Mpanda-Mabwe A, et al. Pantograph-catenary interaction model comparison. IECON 2010 - 36th Annual Conference on IEEE industrial Electronics society; IEEE; 2010, p. 1584–1589.

[44] Jia F, Xu F, Zhou H, et al. Optimization and simulation of the operational motion of a pantograph: uplift and retraction. J Mech Sci Technol. 2017;31(1):41–52.

[45] Ambrósio J, Pombo J. A unified formulation for mechanical joints with and without clearances/bushings and/or stops in the framework of multibody systems. Multibody Syst Dyn. 2018;42(3):317–345.

[46] Bautista A, Montesinos J, Pintado P. Dynamic interaction between pantograph and rigid overhead lines using a coupled FEM — multibody procedure. Mech Mach Theory. 2016;97:100–111.

[47] Liu N, Cui T, Li M, et al. Study of vehicle pantograph-catenary dynamic performance based on ADAMS). 2016 35th Chinese Control Conference (CCC); IEEE; 2016, p. 10150–10155.

[48] Hu C, Wan F. Parameter identification of a model with Coulomb friction for a real inverted pendulum system. 2009 Chinese Control and Decision conference; IEEE; 2009, p. 2869–2874.

[49] Rail pantograph 160 EC [Internet]. Kraków: [cited 2020 Jul 03]. Available from: http://www.en.ec-e.pl.